Optical Characterization of Micro Spiral Phase Plates

Sebastian Buettner, Erik Thieme and Steffen Weissmantel
Laserinstitut Hochschule Mittweida, University of Applied Sciences Mittweida,
Technikumplatz 17, 06948 Mittweida, Germany

Keywords: Fluorine Laser, Fused Silica, Micro Structuring, Orbital Angular Momentum, Spiral Phase Plates.

Abstract: The results of our investigations on laser fabricated micro spiral phase plates in fused silica are presented. Other than in previous investigations we focussed on the optical characterization of the SPPs. As we could show, the laser-based process enables the generation of spiral phase plates with different topological charges, handedness, modulation depths and level numbers. Each geometric property influences the property of a transmitting electro-magnetic field and therefore the orbital angular momentum. For the optical characterization we observed and analysed the diffraction images of the generated SPPs. Moreover, we validated our results by calculating the diffraction patterns under variation of certain parameters.

1 INTRODUCTION

Since Maxwell light is understood in terms of electromagnetic fields. The connection of magnetic and electrical fields led to a new view to photons and light in general. The solution of Maxwell's equations in absence of matter and charges is an electromagnetic wave with the properties, wavelength, polarization, amplitude and phase. All these are used in modern technologies and can be influenced for different purposes and applications. In 1909 Poynting showed, that electromagnetic fields can have spin angular momentum (SAM), which is associated with the circular polarization of an electromagnetic field (Poynting, 1909). In 1992 Allen et. al. proved that Laguerre-gaussian laser modes also got orbital angular momentum (OAM) (Allen et al., 1992). The recognition that light can have angular momentum led to a new understanding and consequently to many new applications. The total angular momentum $\vec{J}$ of an electro-magnetic field can be calculated from the electrical field strength distribution E.

$$\vec{J} = \frac{\epsilon_0}{2i\omega} \underbrace{\int \sum_{j=x,y,z} E_j^* (\vec{r} \times \nabla) E_j \, d^2r}_{\vec{i}} + \frac{\epsilon_0}{2i\omega} \underbrace{\int E^* \times E \, d^2r}_{\vec{s}} \quad (1)$$

As can be seen from equation (1), the SAM is an intrinsic property, whereas the OAM results from a spatial distribution. More precisely, the OAM results from a phase distribution with an azimuthal dependency. The modulation of an even wave front with a helical phase term gives the Poynting vector a helical trajectory (Allen and Padgett, 2011). The idea that the total OAM results from the spatial distribution is correct with respect to the entire field. Counterintuitively, it can be shown that single photons can also have orbital angular momentum. In 2005 Anton Zeilinger's group showed that the OAM states of individual photons can be entangled (Mair et al., 2001). The entanglement of OAM states of single photons enables the development of new quantum technologies with enormous potential (Fickler et al., 2012,2014; Cardano et al.,2015; Krenn et al., 2017).

Moreover, the OAM become interesting for several other applications like optical tweezers and particle manipulation (Grier,2003). However, this property can be used to encode classical information for optical data transfer. In the last years, several methods for creating light and in particular laser beams with a defined OAM were developed. As example, there are some micro-optical elements which can be used to modulate and convert light. One of them is a q-plate, which converts SAM to OAM (Marrucci et al., 2006; Karim et al., 2009). But also phase elements like fork gratings (FGs) and spiral phase plates (SPPs) can be used to influence the OAM of electromagnetic waves, as well as spatial light modulators (SLM) (Zhu et al., 2018; Xie et al., 2018; Bozinivic et al. 2013). In addition to this, FGs and

Buettner, S., Thieme, E. and Weissmantel, S.
Optical Characterization of Micro Spiral Phase Plates.
DOI: 10.5220/0012376400003651

In *Proceedings of the 12th International Conference on Photonics, Optics and Laser Technology (PHOTOPTICS 2024)*, pages 57-64
ISBN: 978-989-758-686-6; ISSN: 2184-4364

SLMs were used to encode data to OAM states and vice versa. To push forward the idea of OAM based data communication, we developed a laser-based technique, which allows the generation of individual micro SPPs in fused silica. In this investigation we focused on the measurement of the optical function of the generated SPPs.

2 SPP PROPERTIES

The OAM of an electromagnetic field is a result of the modulated phase with an azimuthal dependency. A description of such a modulated wave is given in equation (2), where $u(x,y,z)$ represents the amplitude and $e^{il\varphi}$ the phase of the field. The phase depends on the azimuth angle φ and the topological charge l.

$$u(x,y,z) = u(r,\varphi,z) = u_0(r,z) \cdot e^{-ikz} \cdot e^{il\varphi} \quad (2)$$

The modulation can be done using SPPs, which got an azimuthal change in thickness. Due to this, the wave front of a transmitting even electro-magnetic wave becomes a helical shape. For SPPs the topological charge in general represents the number of 2π phase jumps within the structure. Moreover, one can show that the modulation depth also influences the number of intertwined phase fronts in the same way. Due to this, we defined the number of phase jumps as a separate quantity j, as well as the modulation depth m. The resulting topological charge l is given then by equation (3).

$$l = m \cdot j \quad (3)$$

This provides a certain degree of freedom regarding the generation of the SPPs. According to the Huygens law, the effect of j and m differs. Regarding to this, j led to the interaction of the elementary waves of one wave front. Whereas $m > 1$ led to the interaction of the elementary waves of m wave fronts. As result, the modulation depth can act as time delay, due to the delay of interaction of elementary waves of the 1st and the mth wave front. Concluding, the modulation depth induces a time delay from fractional to full modulation. It is unlikely, but it could be necessary to take this in account for some ultra-fast applications. Due to the delay is in a range of few femtoseconds for a typically wavelengths in the micron range. An ideally helical modulated wave front converts a gaussian to a ring-shaped intensity distribution. In the centre of the SPPs is a phase singularity, which occur also in the modulated wave front. Therefore, the intensity in the range of the singularity approaches zero. In Fig. 1 and Fig. 2 the calculated electric field and phase distributions are shown for different distances to the plane of modulation. The calculations were done using the Fresnel-Kirchhoff diffraction integral. The comparison of Fig. 1 and Fig. 2 shows that the modulation depth m and the number of phase jumps j got the same effect. Due to this, the topological charge of the field can be controlled by the modulation depth, the number of phase jumps or both simultaneously. This is beneficial regarding to the generation process, which allows the generation of SPPs with at least two sectors. By stetting m to 0.5 an SPP with a l of 1 can be generated too.

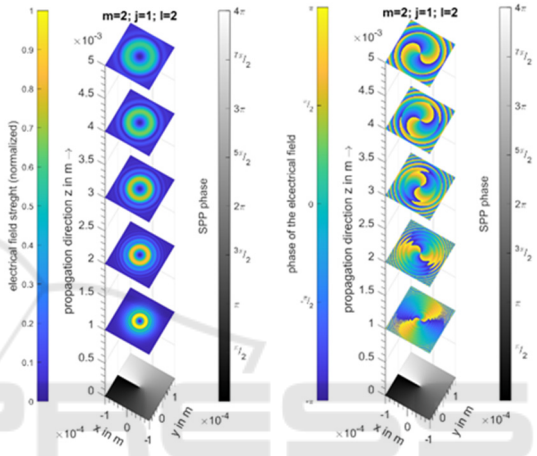

Figure 1: Calculated electrical field strength (l.) and phase distribution (r.) of an OAM beam ($l = 2, j = 1, m = 2$).

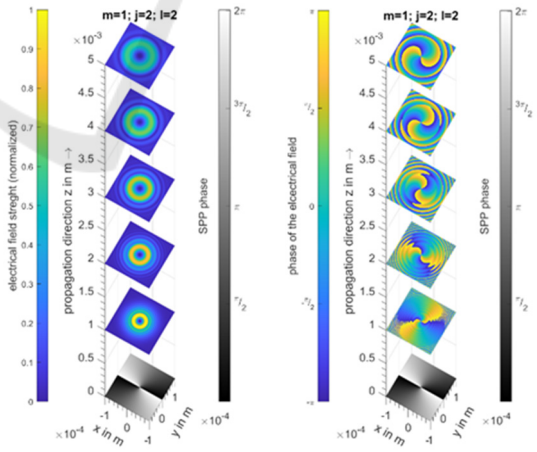

Figure 2: Calculated electrical field strength (l.) and phase distribution (r.) of an OAM beam ($l = 2, j = 2, m = 1$).

Our interest in this field of research and expertise in laser micro structuring of optical materials led us to develop a process for micro SPP generation. The process allows the fabrication of those elements in various versions. For example, Fig. 3 shows one of

the generated SPPs in fused silica. A detailed description of the experimental setup and the process can be found in a former report (Buettner et al. 2020).

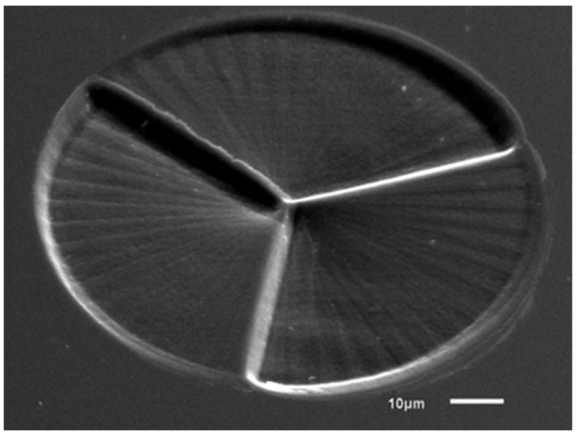

Figure 3: Scanning electron microscope image of a right-handed micro spiral phase plate (j=3, m=2, l=6).

3 RESULTS AND DISCUSSION

For these investigations, we observe and evaluate the diffraction images of the SPPs using the measurement setup that we set up earlier. Due to this, a description of the basic set-up can also be found in the above-mentioned paper. Following, it is also briefly described. The measurement setup consists of a frequency-doubled Nd:YAG laser (λ=532 nm), a series of polarisers, two lenses with different focal lengths (f=175 mm, f=10 mm) and neutral density (ND) filters. With the improved setup the laser spot size can be set to a defined value. Reducing the size of the laser spot requires a reduction in the intensity of the measuring laser to avoid overdriving the camera. This is achieved using two polarisers and additional ND filters. The radius of the frequency-doubled Nd:YAG laser beam is 0.65 mm. This is reduced to 37 µm using the two lenses. The substrate is positioned at the focal point of the second lens. At this point the wavefront is assumed to be flat. Moreover, an XY axis is used to position the SPPs within the measurement laser beam. In this way the SPP can be adjusted concentric to the laser beam. The resulting diffraction images were recorded with a confocal microscope positioned above. The whole microscope can be moved vertically in micron steps, which allows to adjust the distance between the SPP and the plane of observation. This allows the diffraction images to be recorded at different distances from the SPPs. The diffraction images are used to calculate the maximum and root mean square (rms) radius (r_{max}, r_{rms}) of the ring-shaped intensity distributions too, as well as the divergence angle of the propagating fields. For a first measurement we used a laser spot size of 90 µm. Due to the spot size is in the range of the SPP diameter, the modulated and unmodulated components of the transmitting field were interfering strongly, as can be seen in Fig. 4. The generated interferograms show the number and symmetry of the twisted phase fronts in the form of curved intensity maxima. The number of maxima is equal to the topological charge of the corresponding SPP. Moreover, the comparison of the interferograms of SPPs with the same topological charge shows the same number of maxima, due to the modulation depth and the number of phase jumps have the same effect.

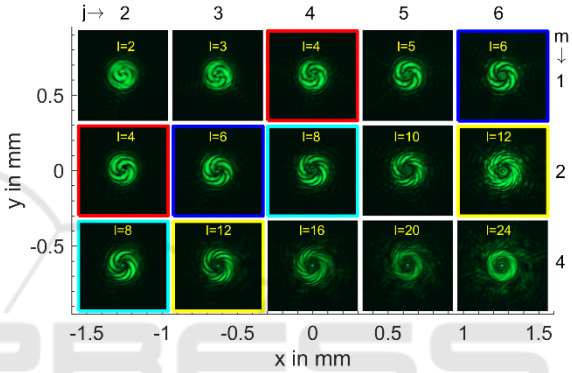

Figure 4: Interferograms of the SPPs with different topological charges, 3 mm above the modulating surface.

The alignment of the SPPs was done by observing the symmetry of the diffraction pattern during the adjustment. Nevertheless, some of the interferograms show asymmetries within the intensity distribution. These deviations result from geometric asymmetries of the SPPs. Moreover, for SPPs with a topological charge >12 the intensity maxima cannot be separated easily. The higher the topological charge, the more the intensity distribution is distorted. This can be explained by a change of the local pitch angle within one sector and the slope edges between the steps of the structures. The change of the local pitch angle is a result of a varying ablation depth per laser pulse during the generation process and it is caused by the fluctuation of the laser pulse energy. The slope angle at the edges of the ablation area depends on the ablation depth per pulse. Due to this, the edges of the steps got a constant slope angle, which depends on the ablation depth and therefore the laser pulse fluence. The local pitch angle of the SPP sector is given by the topological charge, the modulation depth and the distance to the optical axis. Consequently, the slope angle of the step edges mostly does not match the

required local pitch angle of the SPP sector. Increasing the modulation depth by the step number increases the slope area within one sector. These areas contain a different phase information and do not contribute to the targeted phase and intensity distribution. The slope edges got a negative effect on the resulting wave front and increase the losses and distortion within the diffraction image. Furthermore, we observed the diffraction images with a beam radius of $w_0 = 37\ \mu m$ (Fig. 5). For the SPPs with a modulation depth of $m = 4$ the quality of the diffraction images was very low and affected by distortion. In general, the diffraction pattern does not show the expected ring-shaped intensity distributions as shown in Fig. 1 and Fig 2. Instead, the images show intensity maxima, which are surrounded by a ring-shaped distribution with lower intensity. The reason for this is an insufficient phase modulation, due to the total depth of the structures not matching the equivalent 2π, 4π and 8π phase shift (Tab. 1). This also can be shown by the numerical calculations of the diffraction images considering the deviations from the ideal phase. The calculated diffraction images show the same characteristics as the measured (compare Fig. 5 (a) and (b)). Concluding, the deviation of the ideal phase in terms of a systematic deviation from the depth causes a change in the intensity distribution The intensity maxima rinsing with the increase of the deviations.

The reason for the deviations of the structure depths is an insufficient adjustment of the laser pulse fluence. The adjustment was done measuring the laser power near to the image plane of the laser system at a constant frequency of 200 Hz. This is necessary because the laser power must be raised to the measuring range of the power meter. A constant operation of the laser at a defined frequency led to the thermal equilibrium of the laser tube. For the SPP generation a pulse-on-demand operation is necessary. In this mode, the effective laser pulse frequency is in a range of 1 Hz, due to the slow angular velocity of the rotation stages. By changing the operation mode and therefore the laser frequency, the laser is not in a thermal equilibrium anymore and the laser power drops. As result, we reached only 88.5 ± 3.28 % of the targeted depth. This systematic deviation can be avoided improving the measurement for the pulse-on-demand mode or using a power offset.

Table 1: Phase shift of the SPPs, calculated from the measured maximum structure depth.

m / j	2	3	4	5	6
1	1.65π	1.72 π	1.75 π	1.82 π	1.85 π
2	3.50 π	3.63 π	3.69 π	3.67 π	3.77 π
4	6.97 π	6.96 π	6.70 π	6.75 π	6.84 π

However, we calculated the diffraction images for the ideal SPPs with 2π, 4π and 8π phase shift (Fig. 7). The calculation was done using a continuous phase profile. The aperture was set to 150 µm and is therefore twice as large as the beam diameter. This reduces the influence of the aperture on the diffraction image.

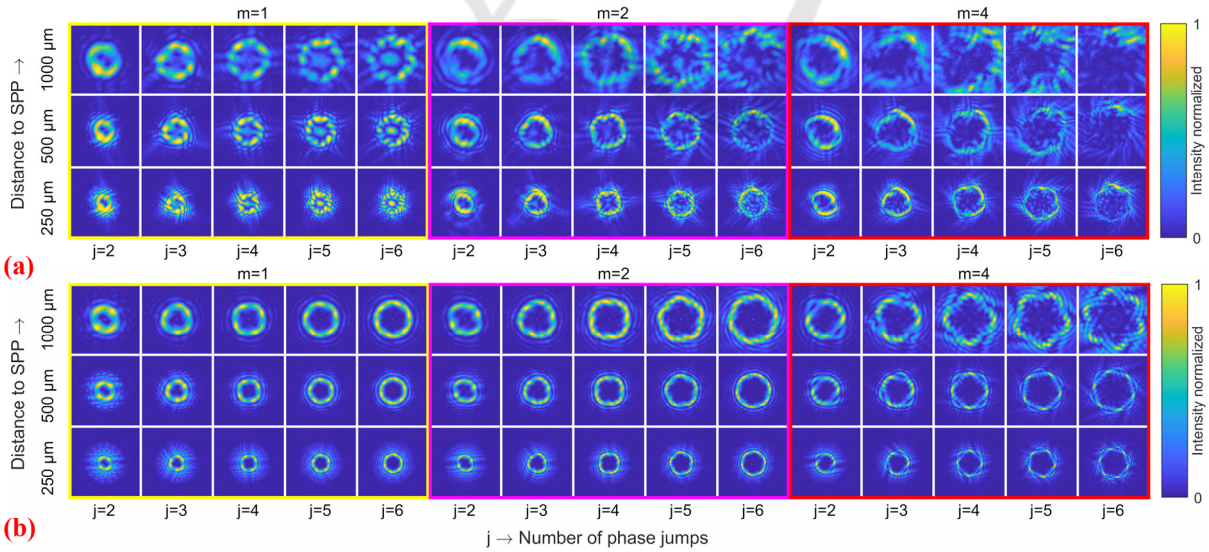

Figure 5: Coloured representation of the measured diffraction images (generated by the SPPs) (a) and the calculated (b) intensity distributions for the appropriate distances ($z = 250\ \mu m$, $500\ \mu m$, $1000\ \mu m$ / $w_0 = 37 \mu m$ / $\lambda = 532\ nm$).

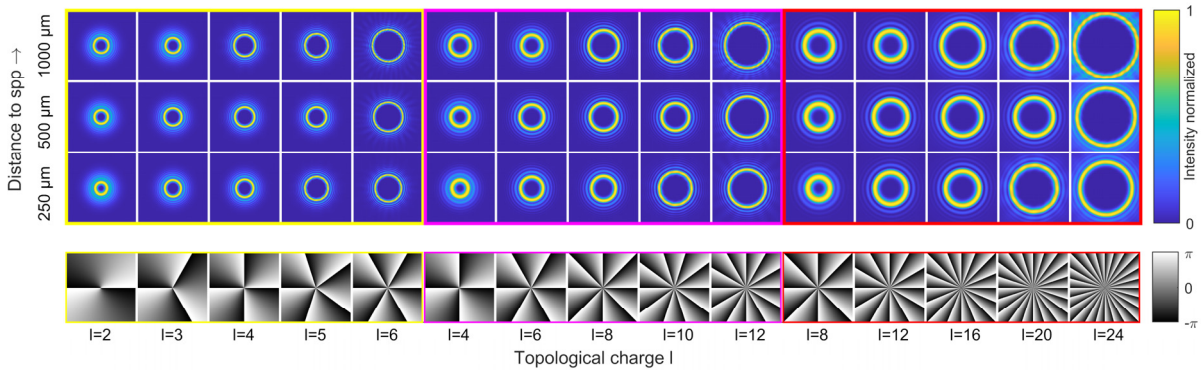

Figure 6: Coloured representation of the calculated intensity distributions (top) using an ideal and continuous phase distributions (bottom) in a distance of 250 µm, 500 µm and 1000 µm to the modulation plane.

Moreover, the size of the target area is changed with the distance, due to the divergence of the field and appropriate increase of the radius of the distribution. The calculation of the ideal diffraction images shows the dependency of the rms and maximum beam radius from the topological charge without the influence of the aperture and steps. The topological charge was varied from 1 to 25 and the modulation depth was set to $m = 1$ for all calculations. According to the target values of the generated SPPs the optimum diffraction images are shown in Fig. 6. The maximum radii r_{max}, were calculated from the 1000 biggest intensity values, using a circular fit function. The rms radius r_{rms} was calculated by the second moment method. As can be seen, both, the rms and the maximum radius increases with the topological charge (Fig. 7.). For small values of the topological charge the maximum and the rms radius depend on l in a very different way. With higher values the course of both radii become more linear.

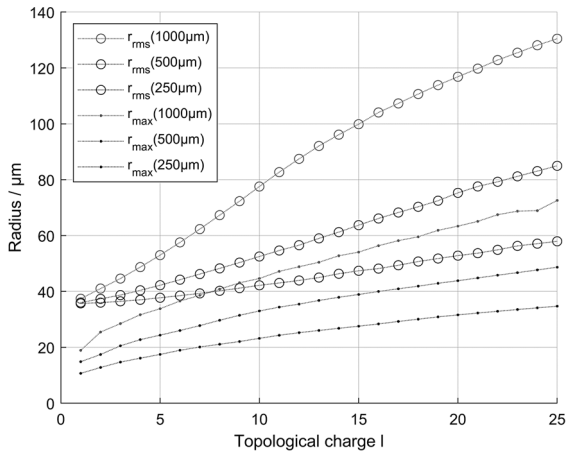

Figure 7: Root mean square (rms) and maximum radii of the calculated ideal intensity distributions depending on the topological charge for different distances z.

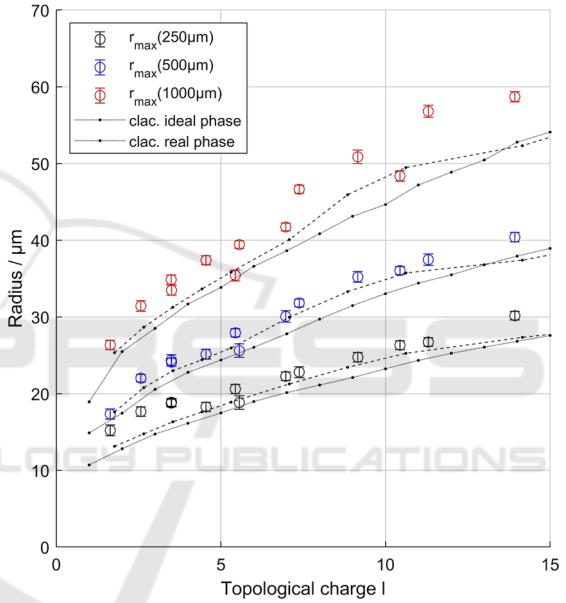

Figure 8: Radii r_{max} of the measured and calculated intensity distribution for different distances in propagation direction. The calculation was done using the ideal phase and determined values for the real SPPs (see Tab. 1).

It can be seen further that the rms radii for $l = 1$ is close to the radius of the input beam waist w_0. The measured maximum radii basically follow the course of the calculated maximum radii (Fig. 8). However, there is a small offset of the measured radii to the calculated, which can be partially explained by the inaccuracy of the phase of the generated SPPs. Taking this into account, the calculated radii approach the measured radii, but a small difference remains. The reason for this could be a slight misalignment of the SPPs in the direction of propagation. Therefore, the wavefront of the measuring beam is not flat, which increases the radii of the intensity distributions and the divergence of the fields.

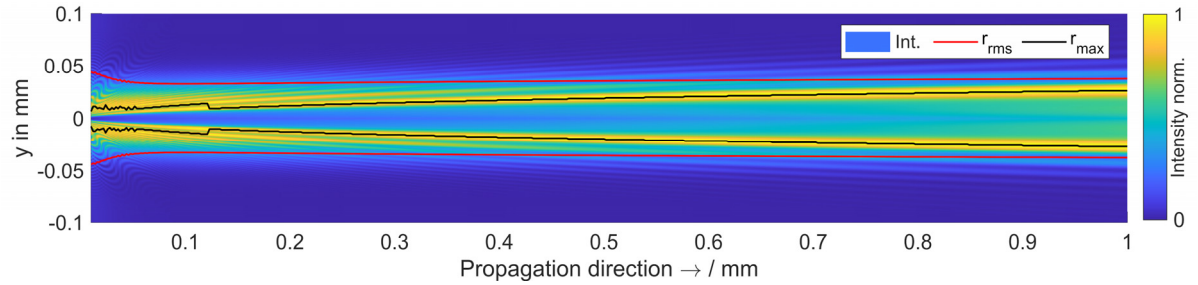

Figure 9: Calculated intensity distribution of an OAM beam ($l = 2$) along the direction of propagation.

For future investigations, the wavefront of the measuring system must be characterized using a wave front sensor. The rms and maximum radii were also compared to theoretical values. Therefore, Padgett and colleagues derived equations for the maximum and rms radius for two different kinds of OAM beams (Padgett et al., 2015). They distinguish between modes with a fixed beam waist (e.g. converting Hermite-Gauss modes into Laguerre-Gauss using a cylindrical lens mode converter) and modulated gaussian modes, which can be generated by illuminating a fork grating. Depending on the mode, a transmitting field propagates differently. Therefore, the far field beam divergence scales either with the square root or linear with the topological charge. Due to the generation of our OAM beams using SPPs, we expect that the beam radius and the divergence depends on the topological charge either in the one or the other way. But it must be taken in account that our measurements and calculations were done somewhat between the near and the far field.

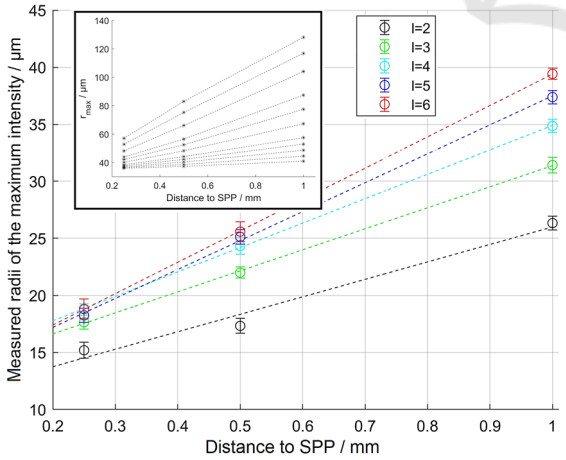

Figure 10: Measured and calculated radii r_{max} of the intensity distributions depending on the distances in propagation direction z.

The equations given by Padgett et al. are valid for the far field. Moreover, the relation between the size and feature size of our generated SPPs and the wavelength got a significant influence on the propagation of the OAM beams, due to the propagation is not transversal at all. This can lead to an abrupt change of the radius of maximum intensity along the propagation axis (see r_{max} in Fig. 9). Due to this, the measured results are valid for these specific structures of this specific size and the mentioned conditions. But the radii do not match the values calculated from the equations, due to the given reason. Fig. 10 shows the measured r_{max} as a function of the distance to plane of modulation for OAM beams with different topological charge. The data fits very well with a linear progression. However, as can be seen from the calculated data, the curve is generally not linear and it also differs depending on the topological charge. Here, investigations with a more precise analysis of the divergence are necessary.

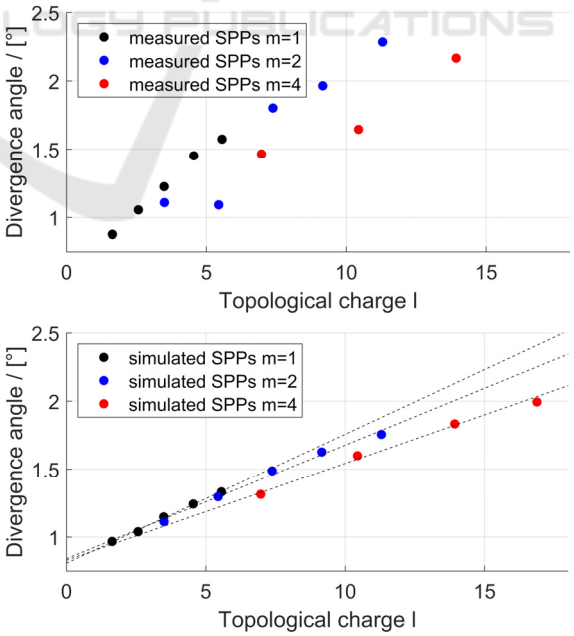

Figure 11: Divergence angle depending on the topological charge calculated from of the measured intensity distributions (top) and the calculated intensity distributions (bottom).

Nevertheless, we calculated the average divergence angle for the measured and calculated intensity distributions (Fig 11.). Both, the measured and calculated angles show a nearly linear dependency regarding to the topological charge. Moreover, the data points are grouped by modulation depth m and the progression between the points of the groups is discontinuous. In addition, each group show a different slope depending on the modulation depth. This shows the influence of the modulation depth on the divergence of the propagating fields, and it must be considered for the design of micro SPPs for a specific application. Concluding, the propagating fields diverge differently depending on the topological charge. In addition to this, the modulation depth also got an influence on the divergence angle. In order to find a general rule for the radii and the divergence of the OAM beams as a function of the topological charge, the further generation and analysis of a large number of high-quality SPPs is necessary. In further investigations, also the influence of the relationship between feature size and design wavelength should be analysed in more detail.

4 CONCLUSIONS

We show the results of our investigations on the optical characterization of laser fabricated micro SPPs. Therefore, we used two measurement configurations. The measured results were verified by numerical calculations of the diffraction images using the Fresnel-Kirchhoff diffraction integral. The captured interferograms show the equality of the modulation depth and number of phase jumps, which act on the topological charge in the same way. Moreover, we captured the diffraction images with a reduced beam radius to supress the interference between the modulated and unmodulated proportion of the propagating field. It could be shown that the calculation in consideration of the geometric properties led to equal diffraction pattern compared to the measured one. This enables us to identify irregularities and asymmetries within the structures and their optical effect.

Simultaneous, we calculated the diffraction images for ideal spiral phase distributions to determine the course of the ideal maximum and root mean square radius of the ring-shaped intensity distributions. The comparison of the maximum radii shows a good fit in course but a small offset of the measured values, due to a small misalignment of the SPPs. Moreover, we determined the divergence angles of the OAM beams, as well as the influence of the topological charge on their divergence. Surprisingly, the modulation depth also got an influence on the divergence of the propagating fields. However, it must be considered that the measurements and calculations were carried out on micro-optics with feature sizes close to the wavelength range. Moreover, the range of measurement is somewhat between the near and far field. Due to this, the far field approximation is not valid. In further investigations, the region of interest therefore should be increased. This may connect our experimental data to the far field approximation.

Finally, the generation process and quality of the micro spiral phase plates must be improved. In particular, the precise control of the laser pulse energy and therefor the ablation depth per pulse can raise the quality of the SPPs significantly. As we have shown, the depth of the structures was not exactly equal to the required equivalent targeted phase shift and the slopes and edges within the structure increased the distortion within the diffraction image. Regarding to this, we currently work on an improved process which will allow us to generate continuous surfaces with arbitrary geometry with highest possible quality.

AKNOWLEDGEMENTS

The authors would like to thank the referees for their careful reading the manuscript and their valuable comments and suggestions. Furthermore, we thankfully acknowledge the financial support from the free state of saxony.

REFERENCES

Poynting, J. H. (1909): The Wave Motion of a Revolving Shaft, and a Suggestion as to the angular momentum in a Beam of Circular Polarized Light.

Allen, L.; Beijersbergen, M. W.; Spreeuw, R. J. C.; Woerdman, J. P. (1992). Orbital angular momentum of light and the transformation of Laguerre-Gaussian laser modes. In: Physical Review A, 45(11), S. 8185-8189.

Allen, L. and Padget, M. (2011). The Orbital angular momentum of light. In Twisted Photons, WILEY-VCH Verlag GmbH, pp. 1-12, Weinheim.

Mair A.; Vaziri, A.; Weihs, G.; Zeilinger, A. (2001). Entanglement of the orbital angular momentum states of photons. In: Nature, 412, pp. 313-316.

Fickler, R.; Lapkiewicz, R.; Plick, W. N.; Krenn, M.; Schaeff, C.; Ramelow, S.; Zeilinger, A. (2012). Quantum Entanglement of High Angular Momenta. Science, 338(6107), 640–643. doi:10.1126/science.1227193

Fickler, R.; Lapkiewicz, R.; Huber, M.; Lavery, M. P.J.; Padgett, M.J.; Zeilinger, A. (2014). Interface between path and orbital angular momentum entanglement for high-dimensional photonic quantum information. Nature Communications, 5:4502., pp. 1-6.

Cardano, F.; Massa, F.; Qassim, H.; Karimi, E.; Slussarenko, S.; Paparo, D.; de Lisio, C.; Sciarrino, F.; Santamato, E.; Boyd, R. W.; Marrucci, L. (2015). Quantum walks and wavepacket dynamics on a lattice with twisted photons. Science Advances, 1(2), e1500087–.

Krenn, M.; Malik, M.; Erhard, M.; Zeilinger, A. (2017). Orbital angular momentum of photons and the entanglement of Laguerre–Gaussian modes. Philosophical Transactions of the Royal Society A: Mathematical, Physical and Engineering Sciences, 375(2087).

Grier, D. A revolution in optical manipulation (2003). Nature 424, pp. 810–816.

Marrucci, L.; Manzo, C.; Paparo, D. (2006). Optical Spin-to-Orbital Angular Momentum Conversion in Inhomogeneous Anisotropic Media. Physical Review Letters, 96(16), pp. 163905–.

Karimi, E.; Piccirillo, B.; Nagali, E.; Marrucci, L.; Santamato, E. (2009). Efficient generation and sorting of orbital angular momentum eigenmodes of light by thermally tuned q-plates. Applied Physics Letters, 94(23), pp. 231124–.

Zhu, L.; Wang, A.; Chen, S.; Liu, J. and Wang, J. (2018): Orbital angular momentum mode multiplexed transmission in heterogeneous few-mode and multi-mode fiber network; In: Opt. Lett. 43, p. 1894-1897.

Xie, Z.; Gao, S.; Lei, T.; Feng, S.; Zhang, Y.; Li, F.; Zhang, J.; Li, Z.; Yuan, X. (2018). Integrated (de)multiplexer for orbital angular momentum fiber communication. In: Photonics Research, 6(7), pp. 743-749.

Bozinivic, N.; Yue, Y.; Ren, Y.; Tur, M.; Kristensen, P.; Huang, H.; Willner, A.E.; Ramachandran, S. (2013). Terrabit-Scale Orbital Angular Momentum Mode Division Multiplexing in Fibers. In: Science, 340(6140), pp. 1545-1548.

Buettner, S., Pfeifer, M., Weissmantel, S., (2020): Fabrication of Micro Spiral Phase Plates in Fused Silica using F2-Laser Microstructuring, *8th International Conference on Photonics, Optics and Laser Technology*.

Padgett, M. J; Miatto, F. M.; Lavery, M. P. J.; Zeilinger, A.; Boyd, R. W. (2015). Divergence of an orbital-angular-momentum-carrying beam upon propagation. New Journal of Physics, 17(2), 023011–. doi:10.1088/1367-2630/17/2/023011